Electronic Supplementary Material (ESI) for Journal of Materials Chemistry A.

Supporting Information

$CuO\text{-}nSnO_2$ reverse cubic heterojunction as high-performance supercapacitor electrodes

Mingyan Chuai, Xi Chen, Kewei Zhang, Jing Zhang and Mingzhe Zhang,*

State Key Laboratory of Superhard Materials, Jilin University, Changchun 130012, People's Republic of China.

*Corrsponding Author: zhangmz@jlu.edu.cn;

Experiment section

Materials characterization

The compositions of samples were investigated by using energy-dispersive X-ray spectroscopy (EDS) attached to a scanning electron microscope (MAagellan-400). Raman spectra were measured with a spectrometer based on a double monochromator equipped with a CCD camera for signal recording (Andor Technology Ltd). The spectra were excited by a solidstate laser (wavelength λ = 473 nm) and measured in the backscattering configuration at room temperature. The appropriate laser radiation power was chosen to provide secure registration of spectra.

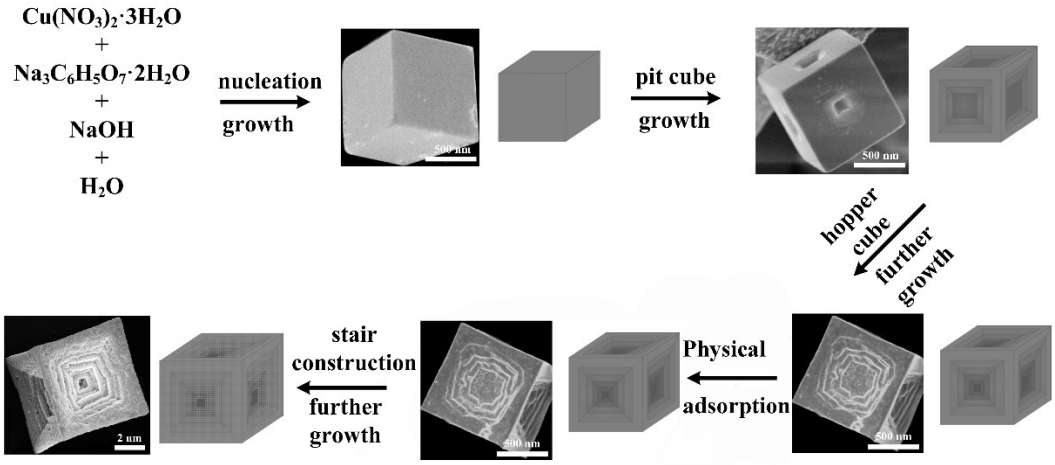

Fig. S1 The growth mechanism schematic of CuO-SnO_2 reverse cubic heterojunctions.

Fig. S1 is the growth mechanism schematic of CuO-SnO_2 reverse cubic heterojunctions. First of all, add the prepared $Na_3C_6H_5O_7·2H_2O$ (12 mmol) and NaOH (4 mmol) solutions into $Cu(NO_3)_2·3H_2O$ (3 mmol) solution, stirring for 2h. Then, the above mixed solution was transferd into a Teflon-lined stainless steel autoclave (50 ml) and transferred into an oven maintained at 200 ℃ for 12 h. The $[Cu_2cit_2H_{-2}]^{4-}$ complexes is formed from cit^{3-} and Cu^{2+} in the mixed solution. In alkaline environment, the $[Cu_2cit_2H_{-2}]^{4-}$ complexes can reduce to Cu^{+} from Cu^{2+} to form Cu_2O. At the beginning of the chemical reaction, the smooth cube structure of Cu_2O are formed according to the mechanisms of REDOX reaction and precipitation reaction. The pit cube structure of Cu_2O and the hopper cube structure of Cu_2O are formed with the increase of the reaction time. The reverse cubic Cu_2O structure can be obtained after the complete reaction. Finally, the CuO-nSnO_2 (n=9 wt%) heterojunctions are obtained by annealing the mixed $SnCl_2·2H_2O$ (6 mg) and Cu_2O (100 mg).

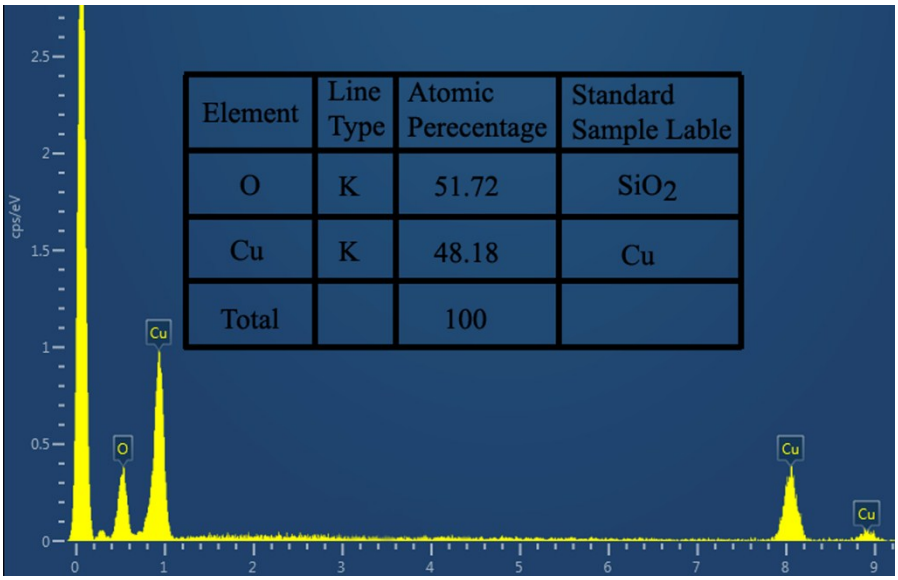

Fig. S2 Energy dispersive X-ray (EDX) spectra of CuO sample. The inset is the composition of each elements of CuO sample.

The EDS spectra only shows the O and Cu elements, which indicates that the synthesized samples are pure phase. The inset shows the composition of each elements of CuO sample. From the table, it can be see that the atomic percent of O and Cu are 51.72% and 48.18%, which illustrates that the ration between Cu atom and O atom is about 1:1. The result indicates that the main body of our synthesized samples is CuO material.

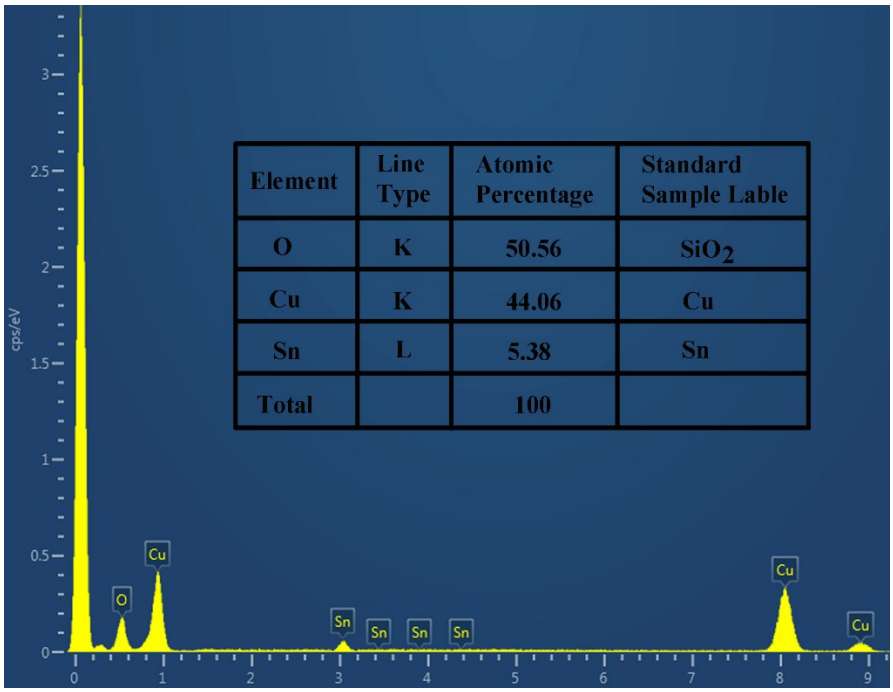

Fig. S3 Energy dispersive X-ray (EDX) spectra of CuO-nSnO_2 (n=9 wt%) heterojunctions. The inset is the composition of each elements of CuO-nSnO_2 (n=9 wt%) heterojunctions.

The EDS spectra only shows the O, Cu and Sn elements, which indicates that the synthesized samples are pure phase. The inset shows the composition of each elements of CuO-nSnO_2 (n=9 wt%) heterojunctions. From the table, it can be see that the atomic percent of O and Cu are 50.56% and 44.06%, which illustrates that the ration between Cu atom and O atom is about 1:1. The result indicates that the main body of our synthesized samples is CuO material. The trace amount of Sn atoms, with an atomic percentage of 5.38%, mainly exists in the structure of SnO_2 materials. The P-n heterojunctions mainly form at the junction between CuO and SnO_2 semiconductors.

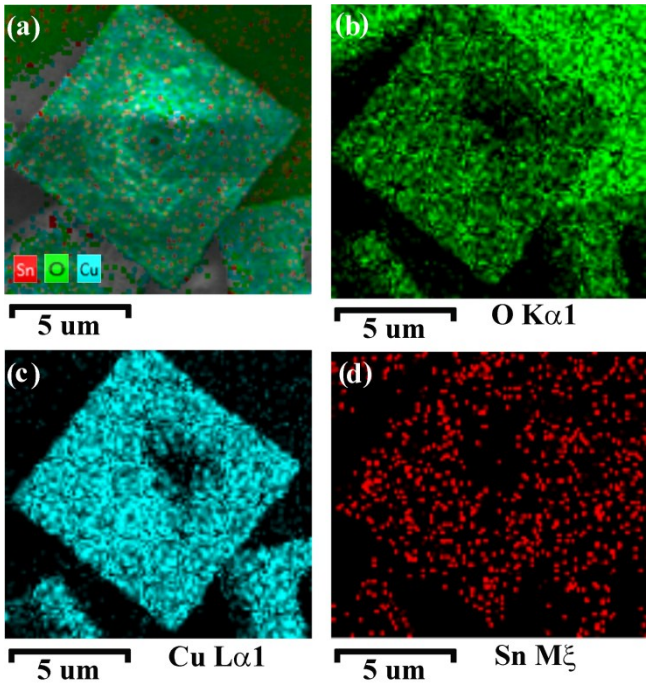

Fig. S4 (a) EDS mapping image of CuO-nSnO_2 (n=9 wt%) heterojunctions. (b), (c) and (d) elemental mapping images of O, Cu and Sn respectively.

It is learn that the distribution of o and Cu elements in Fig. S4 (b) and (c) is well-proportioned. The Sn element is also uniformly distributed in the main structure.

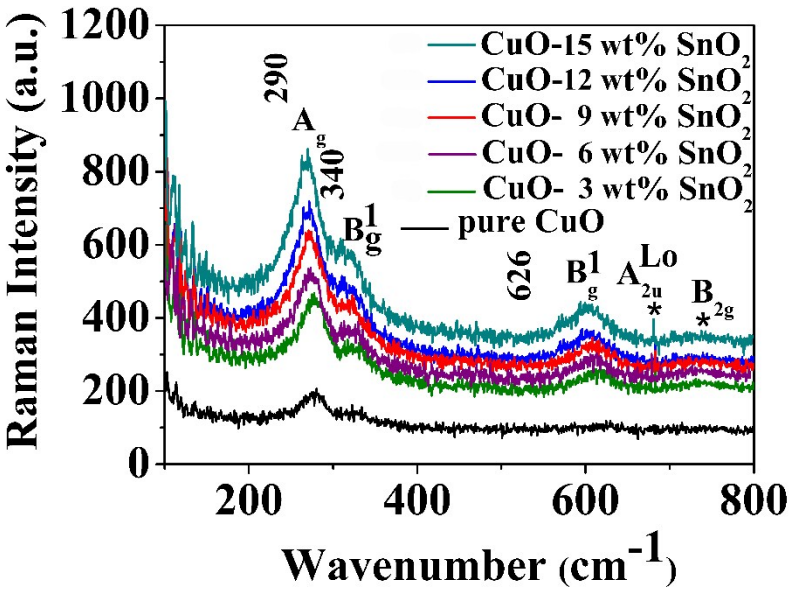

Fig. S5. Raman spectra of pure CuO and CuO-nSnO_2 (n=3 wt%, 6 wt%, 9 wt%, 12 wt%, 15 wt%) heterojunctions at 300K excited by 473 nm radiation from an argon ion laser.

Fig. S5 represents the Raman spectra of CuO-nSnO_2 (n=3 wt%, 6 wt%, 9 wt%, 12 wt%, 15 wt%) heterojunctions. It can be observed that the spectra of CuO and CuO-nSnO_2 (n=3 wt%, 6 wt%, 9 wt%, 12 wt%, 15 wt%) samples represent the bands centered at around 290, 340 and 618 cm^{-1} corresponding to three fundamental active Raman vibration modes A_g, B_{1g}, and B_{2g} of CuO, respectively. For CuO-nSnO_2 (n=3 wt%, 6 wt%, 9 wt%, 12 wt%, 15 wt%) heterojunctions, there are three additional Raman peaks at 632, 696, 775 cm^{-1} corresponding to three fundamental active Raman vibration modes A_{1g}, A_{2u}, and B_{2g} of SnO_2, respectively. Compared to the pure CuO, the Raman peaks of CuO-nSnO_2 (n=3 wt%, 6 wt%, 9 wt%, 12 wt%, 15 wt%) heterojunctions become stronger and broader, and shift slightly to lower wavenumber. Obviously, the peak at 290 cm^{-1} in CuO-nSnO_2 heterojunctions shifts to 285 cm^{-1}, 283 cm^{-1}, 280 cm^{-1}, 278 cm^{-1} and 277 cm^{-1} corespongding to the contents of SnO_2 as 3 wt%, 6 wt%, 9 wt%, 12 wt% and 15 wt%, respectively, and the full width at half-maximum (FWHM) of the peak changing from 40 to 44, 46, 47 and 48 cm^{-1}, respectively, i.e. the blue shift and broadening of the Raman spectra enhanced with the increase of SnO_2. This may be attributed to the semiconductor superlattices and multiple quantum well structures of CuO-SnO_2 heterojunctions. The intensity of the Ranman peaks has significantly enhanced with the increase of SnO_2 concentrations, which indicates the well combination between SnO_2 and CuO.

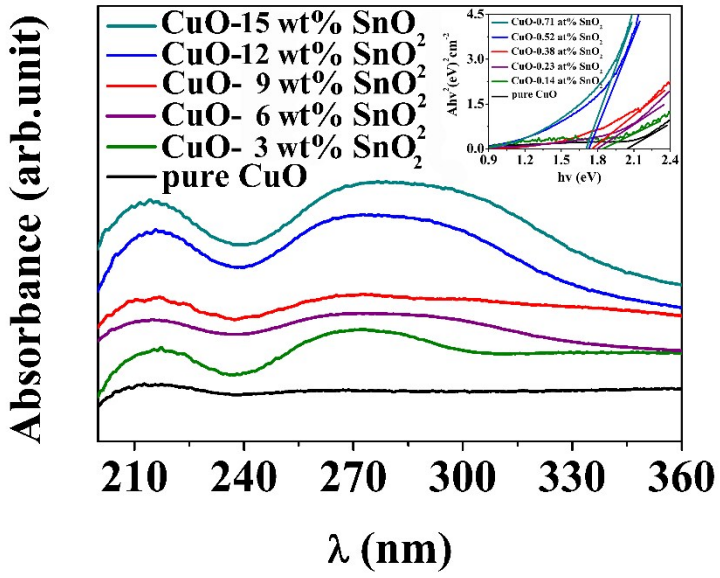

Fig. S6. UV-visible absorption spectra of pure CuO and CuO-nSnO_2 (n=3 wt%, 6 wt%, 9 wt%, 12 wt%, 15 wt%) materials. The inset is the direct band gap energy of all the samples.

Figure S6 shows the UV-visible absorption spectra of pure CuO and CuO-nSnO_2 (n=3 wt%, 6 wt%, 9 wt%, 12 wt%, 15 wt%) heterojunctions at room temperature. It could be noted that the obvious peak located at around 220 nm of all the samples can be attribute to the intrinsic peak of CuO. In addition, the pure CuO has no evident absorption in the region of 240-330 nm, but the CuO-nSnO_2 heterojunctions have obvious absorption between 240 nm and 330 nm, which enhances with the increase of SnO_2 content in CuO reverse cubic samples. It could be used the following relation to calculate the optical energy band gap of the CuO and CuO-nSnO_2 heterojunctions structures:

$(\alpha h\nu)^n = B(h\nu - Eg).$

Where *B* is a constant, *Eg* represents the band gap energy, α is the absorption coefficient, *hv* is the incident photon energy and n is either 2 for a direct band gap energy transition or 1/2 for an indirect band gap energy transition. The direct band gap energy of the CuO and CuO-nSnO_2 heterojunctions structures can be observed in the inset of Fig.3a. The values of the band gap are observed to be 1.96 eV, 1.82 eV, 1.80 eV, 1.79 eV, 1.72 eV and 1.70 eV, corresponding with the SnO_2 concentrations of 0, 3 wt%, 6 wt%, 9 wt%, 12 wt% and 15 wt% respectively. The observed band gap values of pure CuO structures are greater than that of the CuO-nSnO_2 heterojunctions structures which indicates the existence of heterojunctions can effectively shrink the band gap of CuO. The band gap energy of CuO-nSnO_2 heterojunctions structures has been found to significantly decrease when the weight of SnO_2 increase from 3 wt% to 15 wt% in reverse cubic CuO samples. In

general, when the light is absorbed by a material, the electron jumps to the conduction band by leaving a hole in the valance band. From the UV-vis spectrum, the broad absorption peak at around 240-330 nm are remarkably enhanced by increasing the content of SnO_2 in CuO samples. The broad absorption peak may be attributed to the following reasons: (1) the CuO-SnO_2 heterojunctions formed by doping small amount of SnO_2 in CuO may reduce the band gap of CuO and the electrons from the valence band can be excited to the conduction band by absorbing visible light, and (2) the Sn^{4+} ions and Cu^{2+} ions probably exist the similar energy level which is conducive to electronic transition. The direct band gap energy of CuO structure is observed to be 1.96 eV, which is found to decrease down to 1.70 eV with the increasing of heterojunctions content. The Sn^{4+} ions may produce an impurity band into the band gap of CuO by its 4d electrons localized states, which may broaden due to the overlap of the wave functions of the adjacent dopants electrons. This impurity band at can merge with the top of the valence band at the sufficient dopant concentration and may cause the reduction of the band gap.

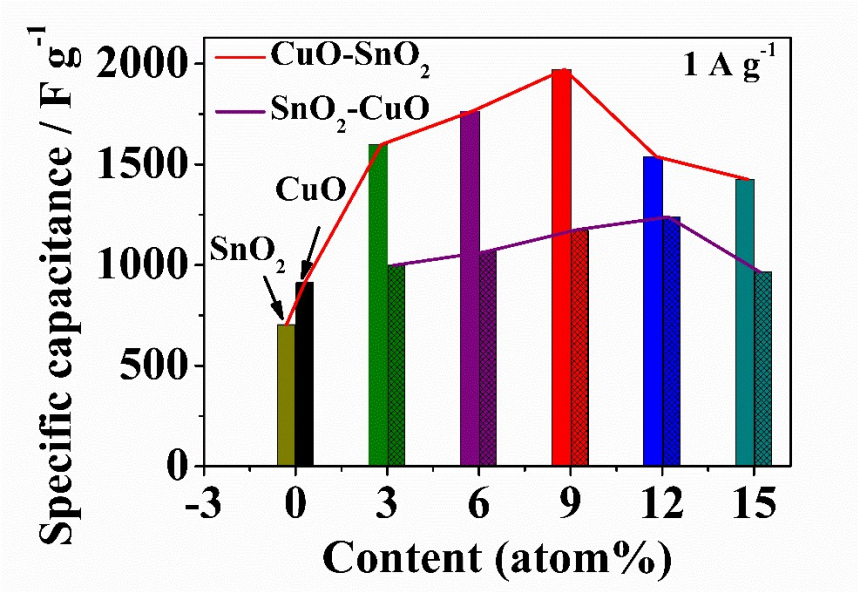

Fig. S7. The specific capacitances for pure SnO_2, CuO, CuO-nSnO_2 (n=3 wt%, 6 wt%, 9 wt%, 12 wt%, 15 wt%) and SnO_2-nCuO (n=3 wt%, 6 wt%, 9 wt%, 12 wt%, 15 wt%) materials at a current density of 1 A g^{-1}.

The specific capacitances of pure SnO_2 and CuO are 704 F g^{-1} and 912 F g^{-1} at a current density of 1 A g^{-1}, respectively. The specific capacitance values of CuO-SnO_2 heterojunctions are 1598 F g^{-1}, 1765 F g^{-1}, 1972 F g^{-1}, 1539 F g^{-1} and 1425 F g^{-1} corresponding the content of SnO_2 as 3 wt%, 6 wt%, 9 wt%, 12 wt% and 15 wt%, respectively. The specific capacitance values of SnO_2-CuO

heterojunctions are 998 F g^{-1}, 1065 F g^{-1}, 1172 F g^{-1}, 1239 F g^{-1} and 965 F g^{-1} corresponding the content of CuO as 3 wt%, 6 wt%, 9 wt%, 12 wt% and 15 wt%, respectively. Obviously, the CuO-nSnO_2 heterojunctions has a higher specific capacitance than that of pure CuO, SnO_2 and SnO_2-nCuO heterojunctions.

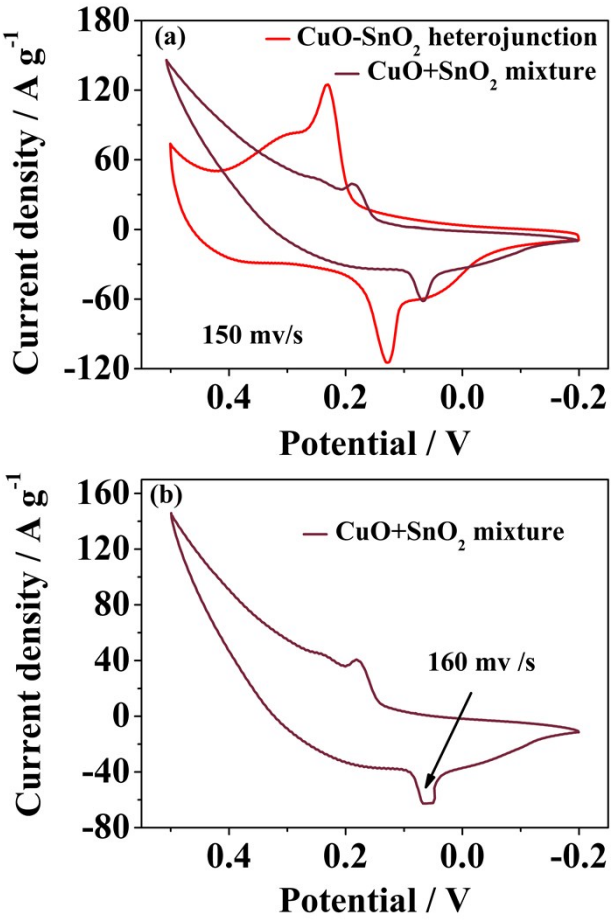

Fig. S8. (a) CV curves of CuO-SnO_2 heterojunction and CuO+SnO_2 mixture at a scan rate of 150 mV/s in 6.0 M KOH. (b) CV curves of CuO+SnO_2 mixture at a scan rate of 160 mV/s in 6.0 M KOH.

To detect whether the high specific capacitance of the CuO-SnO_2 heterojunction are come from the synergistic effects of CuO and SnO_2, the CV curves of the CuO-SnO_2 heterojunction and the CuO+SnO_2 mixture are compared in Figure S8. The red curve is the CV curve of CuO-nSnO2 (n=3 wt%) heterojunctions. The dark red curve is the CV curves of CuO+SnO_2 mixture and the mixture are composed by 9 mg SnO_2 and 100 mg CuO. It can be seen that the high specific capacitance of CuO-SnO_2 heterojunciton is not come from the synergistic effects of CuO and SnO_2. The electrodes of CuO+SnO_2 mixture are punctured at a scan rate of 160 mV/s in 6.0 M KOH. However, the electrodes of CuO-SnO_2 heterojunciton is not punctured at a scan rate of 160 mV/s in 6.0 M KOH.

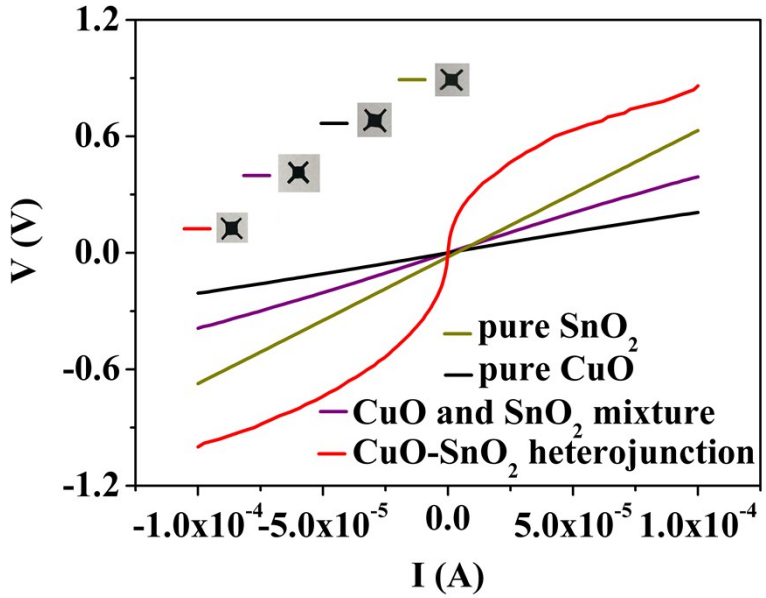

Fig. S9. I-V curves for pure SnO_2, CuO, CuO and SnO_2 mixture, and CuO-SnO_2 heterojunction.

I-V curves of CuO, SnO_2 and the mixture of CuO and SnO_2 are linear, however, the I-V curve of CuO-SnO_2 heterojunction is nonlinear. It was also indirectly indicated that our synthesized samples formed the heterojunction strucutrues.

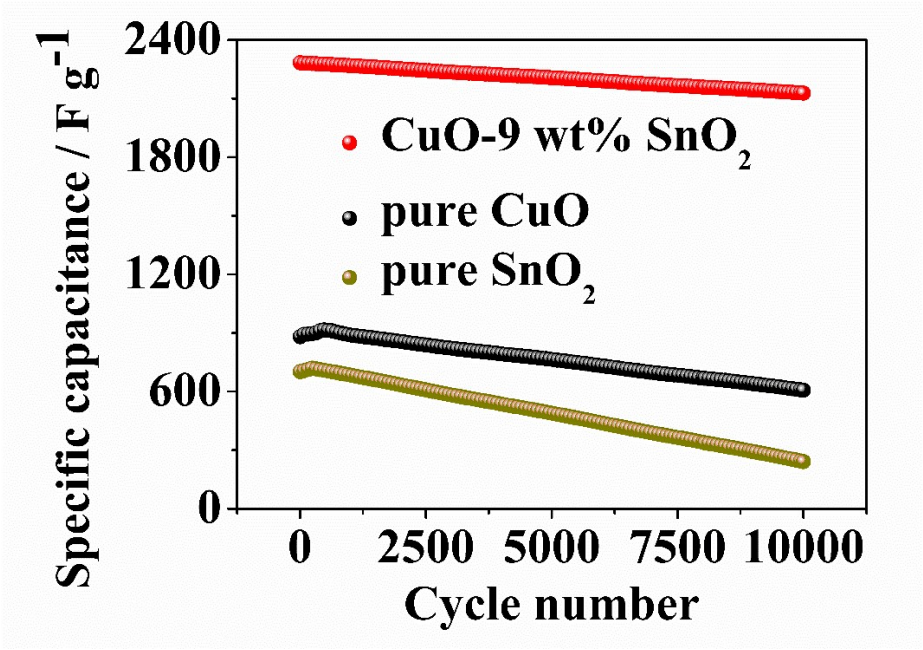

Fig. S10. Cycling performance for CuO, SnO_2 and CuO-9 wt% SnO_2 heterojunctions at 1 A g^{-1} for 10,000 cycles.

Fig. S10 shows the cycling performance for CuO, SnO_2 and CuO-9 wt% SnO_2 heterojunctions at 1 A g^{-1} for 10,000 cycles. The capacitance retention of CuO and SnO_2 are 66.21% and 40.63% after

10,000 cycles respectively, which indicates that the electrochemical stability of CuO and SnO_2 is significantly lower than that of CuO-SnO_2 heterojunctions.

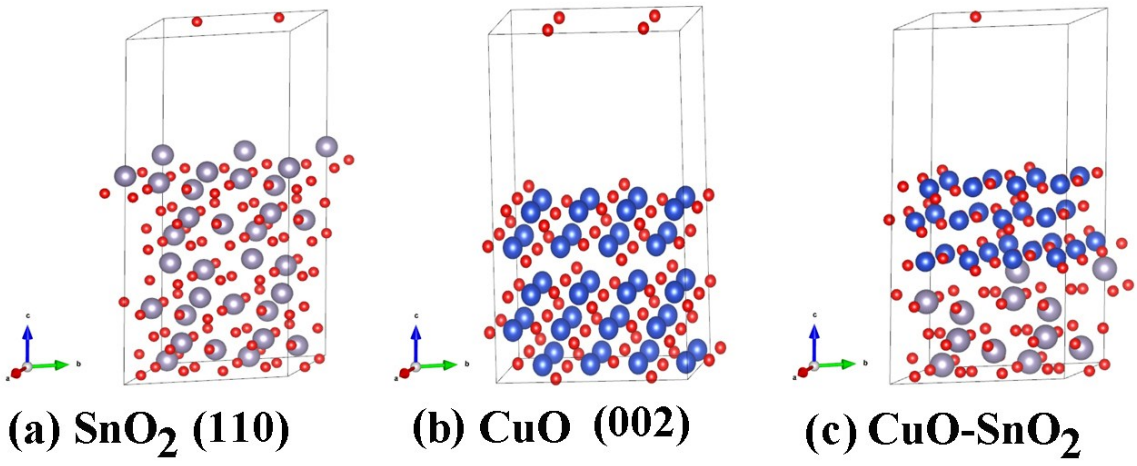

Fig. S11. The models of (a) $Sn_{28}O_{56}$, (b) $Cu_{40}O_{40}$, (c) $Cu_{24}O_{24}$-$Sn_{12}O_{24}$, respectively.

The vectors a, b, and c represent the direction of the lattice constants. The red, blue and gray ball represent the O, Cu and Sn atoms, respectively. The $Sn_{28}O_{56}$ model is the (110) lattice plane structure of SnO_2. The $Cu_{40}O_{40}$ model is the (002) lattice plane structure of CuO. The $Cu_{24}O_{24}$-$Sn_{12}O_{24}$ model is the heterojunction structure of CuO-SnO_2. The supercell model of $Sn_{28}O_{56}$ is obtained by a 2x2x1 expansion of the SnO_2 primitive cell and the supercell structure contains 84 atoms. The supercell model of $Cu_{40}O_{40}$ is obtained by a 2x2x1 expansion of the CuO primitive cell and the supercell structure contains 80 atoms. The $Cu_{24}O_{24}$-$Sn_{12}O_{24}$ model contains 84 atoms. All models have been optimized by VASP.

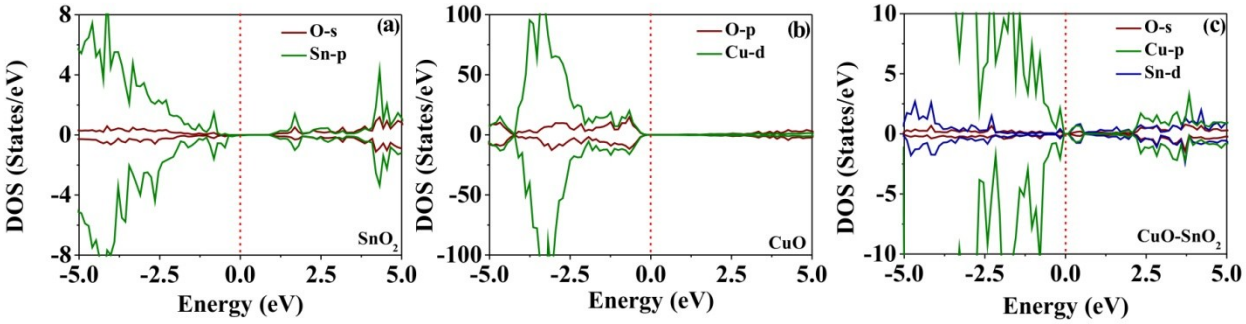

Fig. S12. The PDOS of (a) $Sn_{28}O_{56}$, (b) $Cu_{40}O_{40}$, (c) $Cu_{24}O_{24}$-$Sn_{12}O_{24}$, respectively.

Fig. S12 (a) shows that the SnO_2 structure is mainly s-p orbital hybridization, Fig. S12 (b) illustrates that the CuO structure is mainly p-d orbital hybridization, and Fig. S12 (c) explains that the CuO-SnO_2 structure is mainly s-p-d orbital hybridization.

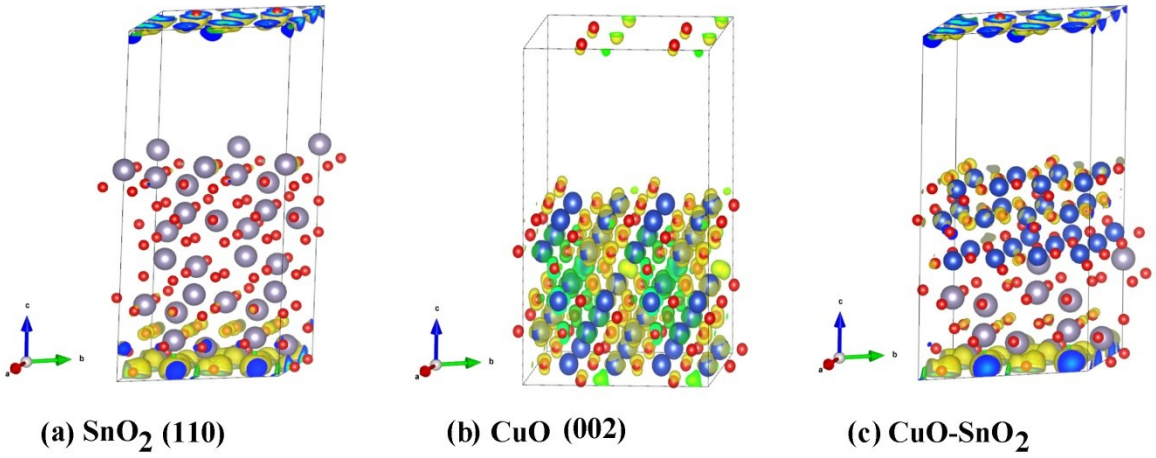

Fig. S13. The 3D spin density diagrams of (a) $Sn_{28}O_{56}$, (b) $Cu_{40}O_{40}$, (c) $Cu_{24}O_{24}$-$Sn_{12}O_{24}$, respectively.

Fig. S13 shows the 3D spin density diagrams of (a) $Sn_{28}O_{56}$, (b) $Cu_{40}O_{40}$, (c) $Cu_{24}O_{24}$-$Sn_{12}O_{24}$, respectively. The yellow isosurface represents the density of electron spin upward and the green isosurface represents the density of electron spin down.

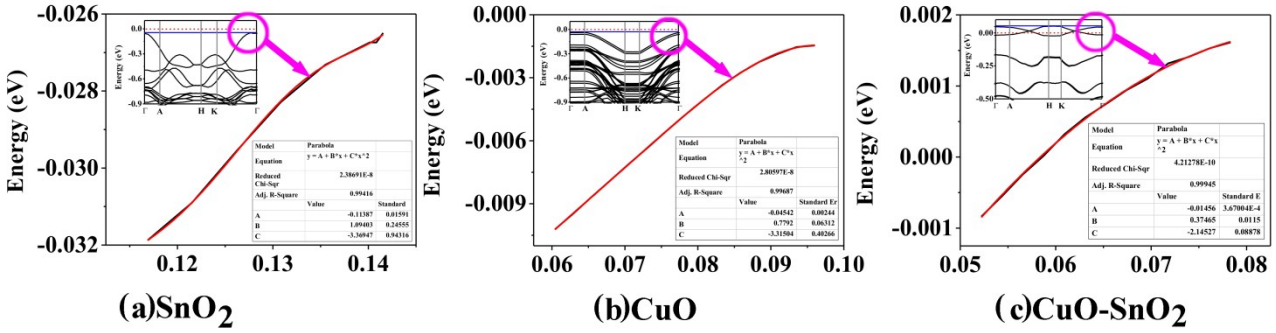

Fig. S14. The electronic effective mass calculation diagrams of (a) SnO_2, (b) CuO and (c) CuO-SnO_2, respectively.

Fig. S14 shows the electronic effective mass calculation diagrams of (a) SnO_2, (b) CuO and (c) CuO-SnO_2, respectively. The red curve in the figure is the fitting curve. The pink circle part in the upper left energy band structure is selected to calculate the electronic effective mass in Fig. S14 (a), (b) and (c). The table in the lower right corner in Fig. S14 (a), (b) and (c) is the parameter corresponding to the fitting data respectively.

Reference

1. J. H. Lin, H. Y. Liang, H. N. Jia, S. L. Chen, J. L. Guo, J. L. Qi, C. Q. Qu, J. Cao, W. D. Fei, J. C. Feng, In situ encapsulated Fe3O4 nanosheet arrays with graphene layers as an anode for high-performance asymmetric supercapacitors, *J. Mater. Chem. A*. 2017, **5**, 24594–24601.
2. R. Patel, J. T. Park, M. Patel, J. K. Dash, E. B. Gowd, R. Karpoormath, A. Mishra, J. Kwak, J. H. Kim, Transition-metal-based layered double hydroxides tailored for energy conversion and storage, *J. Mater. Chem. A.* 2018, **6**, 12–29.
3. M. Kuang, T. T. Li, H. Chen, S. M. Zhang, L. L. Zhang and Y. X. Zhang, Hierarchical Cu2O/CuO/Co_3O_4 core-shell nanowires: synthesis and electrochemical properties, Nanotechnology. 2015, **26**, 304002.
4. R. Ahmad, N. Tripathy, M. S. Ahn, K. S. Bhat, T. Mahmoudi, Y. Wang, J. Y. Yoo, D. W. Kwon, H. Y. Yang and Y. B. Hahn, Highly Efcient Non-Enzymatic Glucose Sensor Based on CuO Modifed Vertically-Grown ZnO Nanorods on Electrode, *Sci. Rep*. 2017, **7**, 5715.
5. M. Huang, Y. Zhang, F. Li, Z. Wang, Alamusi, N. Hu, Z. Wen and Q. Liu, Merging of Kirkendall Growth and Ostwald Ripening: CuO@MnO_2 Core-shell Architectures for Asymmetric Supercapacitors, *Sci. Rep*. 2014, 4, 4518.
6. S. C. Bhise, D. V. Awale, M. M. Vadiyar, S. K. Patil, B. N. Kokare and S. S. Kolekar, Facile synthesis of CuO nanosheets as electrode for supercapacitor with long cyclic stability in novel methyl imidazole-based ionic liquid electrolyte, *J. Solid. State. Electrochem*. 2017, **21**, 2585-2591.
7. P. K. Singh, A. K. Das, G. Hatui and G. C. Nayak, Shape controlled green synthesis of CuO nanoparticles through ultrasonic assisted electrochemical discharge process and its application for supercapacitor, *Mater. Chem. Phys*. 2017, **198**, 16-34.
8. Y. Ko, J. Shim, C. H. Lee, K. S. Lee, H. Cho, K. T. Lee and D. I. Son, Synthesis and characterization of CuO/graphene (Core/shell) quantum dots for electrochemical applications, *Mater. Lett*. 2018, 217, 113-116.
9. S. J. Ki, H. Lee, Y. K. Park, S. J. Kim, K. H. An and S. C. Jung, Assessing the electrochemical performance of a supercapacitor electrode made of copper oxide and activated carbon using liquid phase plasma, *Appl. Surf. Sci*. 2018, **466**, 243-249.
10. S. M. Peng, X. L. Zhu, Y. J. Xing, H. B. Shi, X. Cai, An adaptive state of charge estimation approach for lithium-ion seriesconnected battery system, *J. Power. Sources*. 2018, 392, 48–59.